Available online at www.sciencedirect.com

SciVerse ScienceDirect

Geochimica et Cosmochimica Acta 108 (2013) 141–153

Geochimica et Cosmochimica Acta

www.elsevier.com/locate/gca

Surface charge and growth of sulphate and carbonate green rust in aqueous media

Romain Guilbaud [a,*,1], Maggie L. White [b], Simon W. Poulton [a,1]

[a] *School of Civil Engineering and Geosciences, Newcastle University, Newcastle Upon Tyne NE1 7RU, UK*
[b] *School of Chemical Engineering and Advanced Materials, Newcastle University, Newcastle Upon Tyne NE1 7RU, UK*

Received 16 March 2012; accepted in revised form 16 January 2013; Available online 8 February 2013

Abstract

We report the first determination of the point of zero charge of sulphated and carbonated green rust particles. Green rust has been recognised as a prevalent mineral in environments such as hydromorphic soils, groundwaters and anoxic Fe(II)-rich water bodies, and the evolution of its net surface charge with pH has direct implications for the uptake of contaminants, metals and nutrients in such settings. We find that the surface of both sulphated and carbonated green rust is positively charged at $\text{pH} < 8.3$, whereas it is negatively charged at $\text{pH} > 8.3$. Thus, alkaline settings will promote enhanced adsorption of metallic cations. However, the behaviour of ionic species surrounding green rust is more complicated than that predicted by simple pH-dependent adsorption, as our experiments suggest that green rust likely grows via dissolution–reprecipitation during Ostwald-ripening. This implies that adsorbed species are potentially subject to repetitive steps of release into solution, re-adsorption and co-precipitation during particle growth. The growth rate of green rust particles is highest within the first 50 min of aging, and appears to decrease towards an asymptote after 200 min, suggesting that particle growth controls on the uptake of dissolved species will be most important during the early steps of green rust growth. Our findings thus contribute to a better understanding of the controls that green rust may exert on dissolved ions in a variety of anoxic environments.

1. INTRODUCTION

Most iron oxide and oxyhydroxide minerals are highly reactive in the environment (e.g. Poulton et al., 2004) and play a major role in toxic metal and contaminant remediation (e.g. Waychunas et al., 2005). Amongst these minerals, green rusts have recently been the focus of increasing attention, partly because of the presence of ferrous iron in the structure, which promotes their reducing capability. For example, chlorinated solvents (Erbs et al., 1998; Lee and Batchelor, 2002), nitrate (Hansen and Koch, 1998; Hansen et al., 2001; Choi and Batchelor, 2008) and heavy metals and non-metals such as As^{V} (Randall et al., 2001; Jönsson and Sherman, 2008), Se^{VI} (Myneni et al., 1997) and Cr^{III} (Loyaux-Lawniczak et al., 1999; Williams and Scherer, 2001; Bond and Fendorf, 2003; Legrand et al., 2004) can all be reduced by various forms of green rust. Therefore, green rust may potentially exert a key control on the mobility of ions, the redox cycling of metals, and the degradation of organic and inorganic pollutants in the environment.

The structure and composition of green rust has been widely documented (e.g. Refait et al., 1998; Génin et al., 2001; Ruby et al., 2003; Simon et al., 2003), and consists of brucite-like mixed Fe(II)/Fe(III) tri-octahedral hydroxide layers which alternate with negatively charged interlayers containing planar (CO_3^{2-}, Cl^-) or tetrahedral (SO_4^{2-}) anions. The occurrence of these different anions in the structure defines two distinct minerals, green rust 1 (containing CO_3^{2-} or Cl^-) and green rust 2, (containing SO_4^{2-}). Simon et al. (2003) showed that sulphated green rust 2 (herein referred as GRSO_4) is arranged in a hexagonal geometry, differing with the rhombohedral type 1 green rust

---

* Corresponding author.
E-mail address: r.j.guilbaud@leeds.ac.uk (R. Guilbaud).

[1] Present address: School of Earth and Environment, University of Leeds, Leeds LS2 9JT, UK.

0016-7037/$ - see front matter © 2013 Elsevier Ltd. All rights reserved.
http://dx.doi.org/10.1016/j.gca.2013.01.017

(herein referred as $GRCO_3$), although both display positively charged $[Fe^{II}_4Fe^{III}_2(OH)_{12}]^{2+}$ hydroxide layers.

In the environment, the formation of green rust is not uncommon and the mineral has been found in association with microbial communities and various mineral assemblages. Since its first identification as a corrosion product of steel water pipes (Stampfl, 1969), authigenic occurrences of green rust have been reported in soils (e.g. Trolard et al., 1997; Abdelmoula et al., 1998), groundwaters (Christiansen et al., 2009) and an anoxic Fe-rich lacustrine water column (Zegeye et al., 2012). Because green rusts are mixed Fe(II)–Fe(III) species, the roles of abiotic and biotic redox reactions in their formation has been investigated. *Shewanella putrefaciens* cultures can use Fe(III) mineral species as electron acceptors to form green rusts (e.g. Ona-Nguema et al., 2001; Zegeye et al., 2007a). Green rusts have also been observed during Fe(II) oxidation by nitrate reducing bacteria (Pantke et al., 2011) and during an oxygenic photoferrotrophy (Kappler and Newman, 2004), while $GRSO_4$ can be used as a sulphate source and electron acceptor during bacterial sulphate reduction (Zegeye et al., 2007b). Green rust can also form abiotically by partial oxidation of $Fe(OH)_2$ (e.g. Schwertmann and Fechter, 1994; Refait et al., 1997, 1998; Randall et al., 2001) or steel (e.g. Stampfl, 1969; Świetlik et al., 2012), by partial reduction of ferrihydrite or lepidocrocite (Hansen, 1989), by reaction of $Fe(II)_{aq}$ with ferrihydrite, goethite or hematite (Usman et al., in press), and by co-precipitation of $Fe(II)_{aq}$ and $Fe(III)_{aq}$ under anoxic conditions (e.g. Géhin et al., 2002; Ruby et al., 2003; Bocher et al., 2004; Ruby et al., 2006a,b; Ahmed et al., 2010; this study).

Despite the increasing knowledge of biotic and abiotic green rust formation mechanisms, and of the evident interactions between green rust and metals or contaminants, little is known about the surface chemistry and evolution of green rust particles in aqueous media. This is due to the high reactivity towards oxidation by molecular oxygen, and due to green rust metastability, which makes it difficult to experimentally assess the properties of green rust. In this contribution, we report experimental insight into fundamental aspects of the surface properties of green rust particles. In particular, we demonstrate the mechanism of green rust particle growth in solution, and provide the first determination of the particle surface charge as a function of pH.

2. EXPERIMENTAL METHODS

2.1. Reagents

Experiments were conducted under CO_2-free, oxygen-free conditions (<1 ppmv O_2) in a re-circulating anoxic cabinet (Coy Laboratory Products Inc.®). A 98% N_2 + 2% H_2 atmosphere was maintained through time by automatized injection of the gas mixture, while minute amounts of oxygen were scavenged by palladium catalysts. All reagents and acids were of analytical grade and solutions were prepared under oxygen-free conditions using 18.2 MΩ cm deionised water sparged with O_2-free grade N_2 for 20–40 min (Butler et al., 1994). Rigorous exclusion of oxygen is essential because $Fe(II)_{aq}$ and green rusts are prone to oxidation. Solutions were equilibrated with the inert atmosphere and the pH was stable at the beginning of each experiment. Mixed Fe(II)–Fe(III) solutions were made by dissolution of $Fe^{II}SO_4{\cdot}7H_2O$ and Fe^{III}_2 $(SO_4)_3{\cdot}5H_2O$ at a ratio of $x = 0.33$ (where $x = n_{Fe(III)}/[n_{Fe(III)} + n_{Fe(II)}]$) as suggested by Ruby et al. (2003) in order to solely form the stoichiometric $Fe^{II}_4Fe^{III}_2(OH)_{12}SO_4{\cdot}mH_2O$ and $Fe^{II}_4Fe^{III}_2(OH)_{12}CO_3{\cdot}mH_2O$ species. Na_2CO_3 was used as the CO_3^{2-} bearing reagent.

2.2. Precipitation and ageing of $GRSO_4$ and $GRCO_3$

A first set of experiments consisted of the progressive formation of $GRSO_4$ and $GRCO_3$ following the protocol described by Ruby et al. (2003). Fe(II) and Fe(III) ions were co-precipitated in a borosilicate reaction vessel by dropwise addition of a 0.1 M NaOH solution to a 0.05 M Fe solution (100 mL) at a rate of 0.625 mL min^{-1} to form $GRSO_4$(See Supplementary Information 1 for further discussion regarding the potential effect of dissolved Si on GR formation). Similarly, $GRCO_3$ was formed by dropwise addition of a 0.1 M NaOH + 0.2 M Na_2CO_3 mixture (Bocher et al., 2004) or a 0.2 M Na_2CO_3 solution to the 0.05 M Fe solution at a rate of 0.625 mL min^{-1}. Throughout the base addition, pH was monitored, aliquots of the reaction were sampled, and the solids were vacuum filtered pending XRD and TEM analyses in order to check for potential changes in mineralogy.

A second set of experiments consisted of ageing $GRSO_4$ and $GRCO_3$ *in situ* after rapid precipitation. 5 mL of NaOH or Na_2CO_3 was injected into 45 mL of Fe(II)/Fe(III) solution (0.05 M, $x = 0.33$, OH:Fe = 2:1) in serum bottles in order to quantitatively remove Fe from solution as $GRSO_4$ or $GRCO_3$. The solids were collected by vacuum filtration after ageing on various timescales, from 5 min to ~69 h (in the case of $GRSO_4$), and end-member minerals were characterised by XRD.

2.3. Solubility

Our aim here was not to specifically investigate the solubility of green rust, which would require a completely different study. Instead, our aim was to determine the balance between adsorbed and desorbed protons at the surface of $GRSO_4$ and $GRCO_3$ as a function of pH, and therefore the point of zero charge (PZC) for each mineral in aqueous solutions. However, during proton titrations, a portion of the green rust may dissolve, depending on the pH. This mineral dissolution consumes protons and thus it is important that this consumption is not included in our determination of "sorbed protons" during the PZC measurement. Therefore, it is critical to estimate the concentration of H^+ consumed during such dissolution.

The solubility equations for "anhydrous" $GRCO_3$ and $GRSO_4$ can be expressed as follows (Eqs. (1) and (2)):

$$Fe_6(OH)_{12}CO_3 + 13H^+ = 4Fe^{2+} + 2Fe^{3+} + HCO_3^- + 12H_2O \tag{1}$$

$$Fe_6(OH)_{12}SO_4 + 12H^+ = 4Fe^{2+} + 2Fe^{3+} + SO_4^{2-} + 12H_2O \tag{2}$$

The associated solubility constants have been documented by Rickard and Luther (2007) to be, log $K = 39.1$ and log $K = 3.9$, respectively, based on the potentiometric determination of the free energy of formation (Drissi et al., 1995; Refait et al., 1999). In fact, poorly soluble ferric iron may precipitate as secondary solid phases such as lepidocrocite or goethite, and the overall reactions will reflect an incongruent solubility where solids coexist, as described by Eqs. (3) and (4) for the formation of ferric oxyhydroxide (FeOOH)

$$Fe_6(OH)_{12}CO_3 + 7H^+ = 4Fe^{2+} + 2FeOOH + HCO_3^- + 8H_2O \quad (3)$$

$$Fe_6(OH)_{12}SO_4 + 6H^+ = 4Fe^{2+} + 2FeOOH + SO_4^{2-} + 8H_2O \quad (4)$$

Depending on which reaction governs green rust solubility during the titrations, total $[Fe(aq)_T]$ in the supernatant will vary, whereby 1 mol of green rust is equivalent to 6 mol of $Fe(aq)_T$ for Eqs. (1) and (2). For Eqs. (3) and (4), however, 1 mol of green rust is equivalent to 4 mol of dissolved $Fe(aq)_T$ and 2 mol of FeOOH. Therefore, we measured total $[Fe_{aq}]$ in the supernatant throughout the experiment. Aliquots of the solution were sampled during proton titrations (ranging from pH 9 to 7.5), filtered through a 0.45 μm membrane Millipore™ filter, and filtrates were acidified with a few drops of concentrated H_2SO_4 for subsequent spectrophotometric $[Fe(aq)_T]$ determination. When smaller sized filters were used, particles tend to clog off the filter and we preferred using 0.45 μm membranes as both filter sizes gave identical results. We suspect that it is the propensity of GR particles to flocculate that produces individual flocks which are large enough to be trapped on a 0.45 μm membrane filter.

2.4. Potentiometric determination of the PZC

PZC determination of mineral suspensions is usually derived from electrokinetic studies or potentiometric titrations. Wolthers et al. (2005) compared the PZC of iron sulphides obtained by proton titrations (Widler and Seward, 2002; Wolthers et al., 2005) to the isoelectric point obtained using electrophoresis (e.g. Bebié et al., 1998) and concluded that electrokinetic studies may result inoxidation of reduced mineral species. This suggests that the surface of oxygen sensitive minerals may be “refreshed” by proton dissolution during anoxic potentiometric titrations, and thus needs to be considered with respect to green rust.

The principal difficulty in using potentiometric titrations for green rust is its rapid conversion to other mineral phases, because OH^- addition leads to the formation of magnetite and H^+ dissolution may form ferrihydrite or goethite (see below for the mechanisms of green rust formation). It is thus essential to (i) perform the titration within the narrowest pH range possible; (ii) account for protolytic compounds in the solution; and (iii) account for green rust solubility and H^+ consumption during mineral dissolution. We constrained the pH domain of the PZC using the experimental approach described by Ahmed and Maksimov (1969) and Tewari and McLean (1972). A weighed amount of solid was added to a nitrate electrolyte (0.006, 0.01, 0.04, 0.1, 0.5 or 0.7 M KNO_3) of known pH, and any subsequent pH change was tracked over 6 min (as suggested by Tewari and McLean, 1972). NaCl was avoided as it may have promoted the formation of chlorinated green rust. The rates of nitrate reduction by $GRSO_4$ and $GRCO_3$ are slower than those observed using chlorinated and fluorinated green rusts (e.g. Hansen et al., 2001; Choi et al., 2012), and there was no evidence for ammonium production during our experiment (See Supplementary Information 2 for further discussion regarding the potential nitrate reduction in our experiment).The procedure was repeated using starting electrolytes of various pH. An apparent pH_{PZC} value is obtained when pH remains constant after mineral addition.

Although this approach can point towards the PZC value, it does not take into account any matrix or dissolution-consuming H^+ effects. Therefore, two titrations were performed in 0.01, 0.04, 0.1, 0.5 or 0.7 M $KNO_3$with*in situ* precipitated $GRSO_4$ and $GRCO_3$ or with solid $GRSO_4$ and $GRCO_3$ added to the electrolyte. In both cases green rust concentrations were ~5 g L^{-1}. The solution pH was allowed to stabilise before HCl (0.02 M) addition (usually <15 min), and the titration was performed from pH 9 to 7.5 to (i) prevent back precipitation when increasing the pH, and (ii) maintain the experiment at a pH below the domain of magnetite formation (see Sections 3.1 and 3.2). Blank titrations were performed from pH 9 to 7.5 on the supernatant (pH 9) collected after filtration using a 0.45 μm membrane Millipore™ filter. In this way matrix effects were taken into account. However, this blank titration does not account for effects due to mineral dissolution and solubility equilibration during the pH 9–7.5 titration, as the ionic background may change when pH decreases. Hence, solubility data were used to correct for these effects. For each measured pH, the charge balance at the mineral surface, Q (in mol g^{-1}), was calculated using Eq. (5):

$$Q = \frac{C_A - C_B - (C_{A_{blank}} - C_{B_{blank}} - [H]^+ + [OH]^-) - [H^+]_c}{m} \quad (5)$$

where C_A and C_B are the concentrations of acid and base added to the reaction or to the blank, $[H^+]$ and $[OH^-]$ are calculated from the measured pH using the Debye–Hückel activity coefficients, $[H^+]_c$ is the concentration of protons consumed as GR solubility increases (as explained in Section 2.3) and m is the mass of the mineral.

We performed back-titrations from pH 7.5 to 9 to check for reversibility. This showed that depending on the experimental duration, some titration and back-titration curves were poorly matched, suggesting a significant degree of green rust dissolution and precipitation of new Fe phases when the pH increased during the back-titration. This was confirmed by XRD analysis of the solids at the end of the titration, which showed a magnetite component in the XRD spectra. Kapetas et al. (2011) point out the adverse effect of allowing a long equilibration time between each pH step on the reversibility of titrations. Although their inspection of the optimal stability criterion before the next acid/base addition accounted specifically for bacteriological systems, it is possible that similar effects occur during the titration of metastable phases such as green rust.

We therefore developed a new titration technique in order to minimise the titration duration and to account for all matrix effects in the blank. Here, the titration was performed from pH 9 to 7.8 using increments of 0.2 pH units. $GRSO_4$ and $GRCO_3$ were precipitated in duplicates, and after pH equilibration one replicate was filtered and the supernatant kept for the blank titration. The proton balance was calculated by the difference in acid or base addition to bring the sample and the blank to the desired pH using Eq. (6):

$$Q = \frac{C_A - C_B - (C_{A_{blank}} - C_{B_{blank}} - [H]^+ + [OH]^-)}{m} \quad (6)$$

Using this method, the blank solution accounted for solubility effects and dissolution-consumed H^+ at any pH, since the supernatant was titrated after equilibration between green rust and the solution. We used this time consuming method as a validity check for the titration curves obtained from the previous method.

2.5. Analyses

Total dissolved Fe was measured by UV–Vis spectrophotometry. Solid phases were analysed by X-ray diffraction (XRD) for mineral characterisation, crystallinity and particle average size determination, and by transmission electron microscopy (TEM) for crystallinity and particle size verification.

2.5.1. Spectrophotometry

Filtrates were acidified with a few drops of concentrated H_2SO_4 and treated with potassium permanganate in order to quantitatively oxidise $Fe(II)_{aq}$ into $Fe(III)_{aq}$. Total $[Fe_{aq}]$ (i.e. $Fe(III)_{aq}$) was determined spectrophotometrically using the thiocyanate method at 480 nm (e.g. Vogel, 1951) on a Genesis 6 spectrophotometer (Thermo Spectronic™).

2.5.2. XRD analysis

Directly after filtration, aliquots of the solid phase were coated with a drop of glycerol to prevent oxidation (e.g. Hansen, 1989; Williams and Scherer, 2001; Bocher et al., 2004) and loaded onto a glass sample holder. Fig. 1 illustrates typical XRD scans obtained for $GRSO_4$ (Fig. 1A) and $GRCO_3$ (Fig. 1B). The analysis of a green rust sample was repeated after 8 and 24 h and displayed the same XRD spectrum, inferring that the glycerol coating efficiently prevented oxidation. Samples were analysed on a PANalyticalX'Pert Pro MPD diffractometer using Cu–Kα radiation (characteristic wavelength, $\lambda = 1.5418$ Å) generated at an accelerating voltage of 40 kV and a current of 40 mA in a 5–45° 2θ range, with a 0.0334° 2θ step size. As suggested by Randall et al. (2001), the green rust patterns used for data interpretation where those described by Vinš et al. (1987).

We used the Scherrer equation (Eq. (7)) on the first diffraction peak to determine the average crystallite size:

$$L = k\lambda(\beta\cos\theta)^{-1} \quad (7)$$

where L is the average crystallite dimension perpendicular to the reflecting planes (Warren, 1990), k is 0.91 (Brindley, 1980), λ is the wavelength of the X-rays (0.154 nm for Cu Kα), and β is the full width of the peak at half maximum height (FWHM). Although the Scherrer equation has been used in nanomaterial studies to determine the size of the crystal domain (e.g. Huang et al., 2003; Wolthers et al., 2003; Jeong et al., 2008; Guilbaud et al., 2010), our aim here was to track any difference in L over time. It is not known whether the use of glycerol may have a deteriorating effect on crystallinity and the FWHM. Nevertheless, we did not attempt to provide absolute crystal size but rather aimed to track variations over time. Precision on L is given by the reproducibility between replicates and is ± 1.4 nm (1σ).

2.5.3. TEM analysis

Aliquots of the solid phase were re-suspended in ethanol, and a drop of the solution was loaded and dried on a copper grid. Ethanol was used in order to ensure rapid evaporation and to minimise the air exposure time during the drying process. TEM analysis was performed on a Philips CM100 electron microscope operated at 100 kV.

3. RESULTS

3.1. Formation of $GRSO_4$

We performed the precipitation experiments as described and reviewed by Ruby et al. (2003, 2006a,b) in order to guarantee that we could reproduce the same mechanism of green rust formation, and also obtain the same products. Fig. 2 plots R as a function of pH for the sulphated species and shows very good agreement between our experiments and those of previous studies. Ruby et al. (2003, 2006a,b) proposed a mass balance diagram where observed mineral assemblages are plotted as a function of x and R (with $R = n_{NaOH}/n_{Fe(aq)T}$), and showed that pure green rust forms for $x = 0.33$ and $R = 2$. They showed that for $x = 0.33$, the first mineral phase to form during base addition is a ferric hydroxysulphate salt (i.e. a ferric oxyhydroxide where some of the OH^- ions are substituted by SO_4^{2-}) and when $R = 1$, the solid fraction of the system is only comprised of FeOOH. OH^- substitution by SO_4^{2-} in the surface layer of the ferric oxyhydroxideis then followed by cluster separation from the ferric oxyhydroxide substrate to react with $Fe^{II}(OH)_2$ and form $GRSO_4$,when $R = 2$. Green rust conversion to magnetite and $Fe(OH)_2$ occurs when $R > 2$. The whole mechanism is reflected in the titration curves by the twopH plateaux, and is confirmed by the TEM images that show the transition from $[FeOOH + GRSO_4]$ to $[GRSO_4 + Fe_3O_4$ (magnetite) + possibly $Fe(OH)_2]$ assemblages.

3.2. Formation of $GRCO_3$

We constructed a similar titration graph for $GRCO_3$ as for $GRSO_4$ (Fig. 3A), and compared the results obtained using the 0.1 M NaOH + 0.2 M Na_2CO_3 or the 0.2 M Na_2CO_3-only titrant solutions. Here, the solid assemblage is only comprised of green rust for $R = 4$ (as opposed to $R = 2$ for $GRSO_4$; Fig. 2), since $Na_2CO_3 + H_2O = 2NaOH + H_2CO_3$ (and therefore $R_{Na2CO3} = 2R_{NaOH}$). Unsurprisingly, the 0.1 M NaOH + 0.2 M Na_2CO_3 titrant

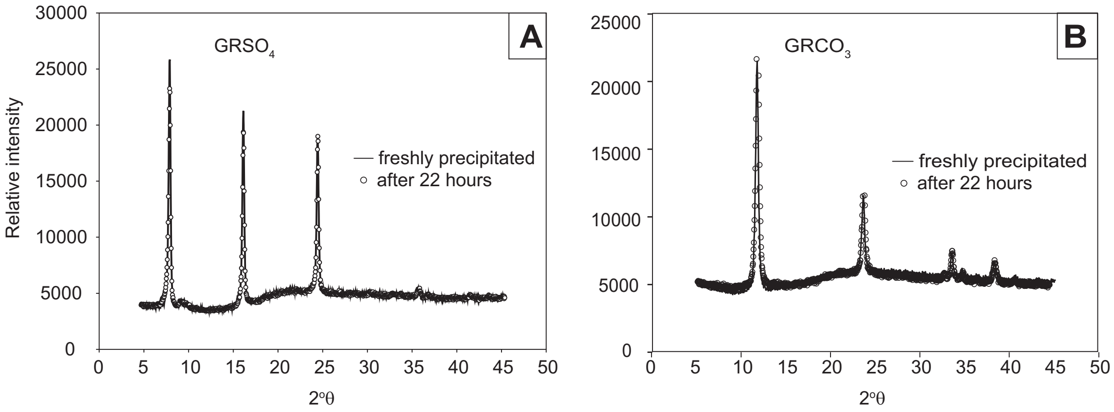

Fig. 1. Typical XRD spectra of freshly precipitated and glycerol-coated GRSO$_4$ (Fig. 1A) and GRCO$_3$ (Fig. 1B). Open circles represent the scan of the same glycerol-coated sample re-analysed after 22 h outside the anoxic cabinet. The similarity of the scans highlights the efficiency of glycerol to prevent oxidation.

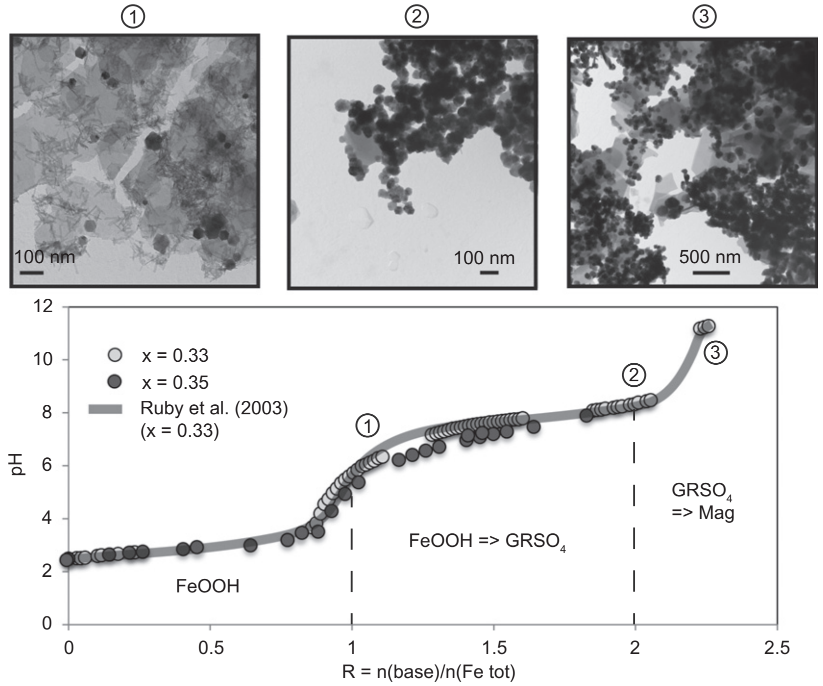

Fig. 2. Evolution of pH *versus* the relative amount of titrant added during the formation of sulphated green rust. Light grey circles represent the experimental data obtained starting with $x = 0.33$. Darker circles were obtained starting with $x = 0.35$. Our data are in good agreements with previous work (light grey curve). The two red crosses indicate the points where the reaction was sub-sampled and the solid products analysed by TEM. At pH 6.5, solid products consist of a mixture of green rust hexagons and lepidocrocite/goethite spikes. At pH 10.2, green rust hexagons have partially transformed to darker magnetite crystals.

brings the system towards higher alkalinity than for 0.2 M Na_2CO_3 alone, and when $GRCO_3$ is formed, there is a difference of more than 2 pH units between the two experiments (Fig. 3A). We found the higher pH system much less stable than when using Na_2CO_3 only, as green rust rapidly transformed into magnetite, and we thus preferred to use the Na_2CO_3-only solution for subsequent experiments.

The difference between the $GRCO_3$ (Fig. 3) and the $GRSO_4$ (Fig. 2) formation graphs lies in the presence of a supplementary transformation for $GRCO_3$as$R$ increases. In fact, XRD analysis of the solid phase throughout the titration revealed that although Na_2CO_3 was used and not NaOH, $GRSO_4$was still forming (Fig. 3B). This is due to the high proportion of sulphate (the starting Fe(II) and Fe(III) source are both iron sulphate salts) in the solution compared with CO_3^{2-} at the start of the progressive base addition. The additional plateau reflects $SO_4^{2-} - CO_3^{2-}$ substitution when CO_3^{2-} becomes the dominant anion.

Using Mössbauer spectroscopy, Ruby et al. (2003, 2006a,b) showed that when $R_{NaOH} > 2$ (similarly, when

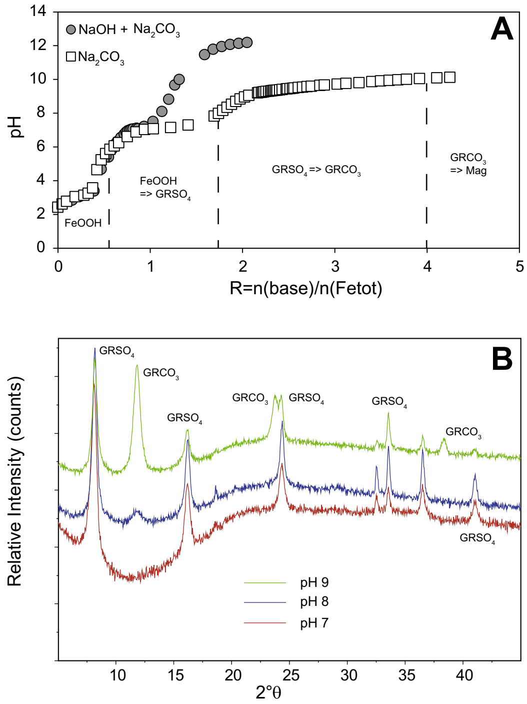

Fig. 3. Evolution of pH *versus* the relative amount of titrant added during the formation of carbonated green rust (Fig. 3A) using different titrant solutions. During the titration, $GRSO_4$ is the first green rust species to form as indicated by the red spectrum (Fig. 3B, pH 7). Anion substitution, i.e. $GRSO_4$ to $GRCO_3$ conversion, starts when $[CO_3^{2-}] > [SO_4^{2-}]$.

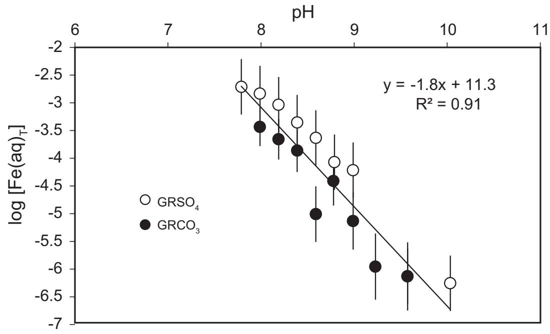

Fig. 4. Total dissolved $[\mathrm{Fe(aq)_T}]$ plotted against pH for both green rust species. The dependence of log $\mathrm{Fe(aq)_T}$ upon pH is supported by the coefficient of determination ($R^2 = 0.91$) on the regression line.

$R_{Na2CO3} > 4$), green rusts rapidly convert to magnetite and $Fe(OH)_2$. The equation can be written as an acid–base reaction (Eq. (8)):

$$\mathrm{Fe_4^{II}Fe_2^{III}(OH)_{12}CO_3 + OH^-} \\ \mathrm{= Fe_1^{II}Fe_2^{III}O_4 + 3Fe(OH)_2 + HCO_3^- + 3H_2O} \qquad (8)$$

Ferrous hydroxide is poorly crystalline in aqueous media, and we could not detect its presence in the XRD spectrum of the end products. Alternatively, the common anoxic $Fe(OH)_2$ to magnetite conversion (the so-called "Schikorr reaction"; Schikorr, 1933) may take place and the overall reaction is (Eq. (9)):

$$\mathrm{Fe_6(OH)_{12}CO_3 + OH^- = 2Fe_3O_4 + H_2 + HCO_3^- + 5H_2O} \qquad (9)$$

3.3. Solubility

Total dissolved Fe measured during the course of the titrations performed on *in situ* precipitated GR shows some dependency on pH for both $GRCO_3$ (using 0.01 M KNO_3) and $GRSO_4$ (using 0.04 M KNO_3). Fig. 4 shows that although the duplicate analysis gave a poor precision (maximum ± 0.5 log $\mathrm{Fe(aq)_T}$), log $[\mathrm{Fe(aq)_T}]$ tends to plot linearly as a function of pH, with a slope of ~−1.8 for both mineral species. It is possible that the apparent shift between the two plots may be due to different solubility products using different electrolyte concentrations. However, the given precision does not permit us to strictly differentiate between the $GRCO_3$ and the $GRSO_4$ results. A broader examination of the plot gives us some indication on the mechanism that governs GR solubility in our experiment. Reaction constants K for Eqs. (1) and (2) can be written as (Eqs. (10) and (11)):

$$K = \frac{[\mathrm{HCO_3^-}][\mathrm{Fe(aq)}_T]^6}{[\mathrm{H^+}]^{13}} \qquad (10)$$

$$K = \frac{[\mathrm{SO_4^{2-}}][\mathrm{Fe(aq)}_T]^6}{[\mathrm{H^+}]^{12}} \qquad (11)$$

Isolating $[\mathrm{Fe(aq)_T}]$ in these equations gives a pH dependent linear equation where $\log[\mathrm{Fe(aq)}_T] \approx \frac{1}{6}\log\frac{K}{[\mathrm{anion}]} - 2$ pH, and therefore the slope would be ~−2 in a log $[\mathrm{Fe(aq)_T}]$ *versus* pH plot. Similarly, for Eqs.3 and 4, the slope would be ~−1.6. Note that the intervention of $\mathrm{Fe(III)_{aq}}$ complexes such as $Fe(OH)_2^+$ would display even lower slopes, around ~−1.5, and the formation of stoichiometric ferrihydrite (Fe_5HO_8 $4H_2O$) would either be pH independent or would display a slope of −1. Our data suggest that during the pH 9–7.5 titrations, a small fraction of FeOOH solids may contribute to the reaction, but ferrihydrite is unlikely to be present. The PZC for freshly precipitated goethite has been determined to be 9.3 ± 0.1 (Antelo et al., 2005), implying that throughout our titrations, the surface of potential FeOOH solids is positively charged, minimising any H^+ adsorption effect. Instead, in their model using phosphate as an adsorbed species, Antelo et al. (2005) suggest that for a pH range of 7.8–9, non-protonated phosphate complexes largely dominate the inner-sphere species. Therefore, the positively charged goethite particles sites are fully compensated by non-protonating anions and no further H^+ adsorption is likely to occur. One could argue that the linearity discussed above is in fact a combination of an ~-2 slope correlation line for pH > 8 and a lower slope correlation line for pH < 8. This may indicate that incongruent dissolution of green rust only takes place at lower pH, implying that green rust is the only solid phase from pH 9 to 8. The very high green rust concentration used in our experiments (~5 g L^{-1}) suggests that the green rust surface

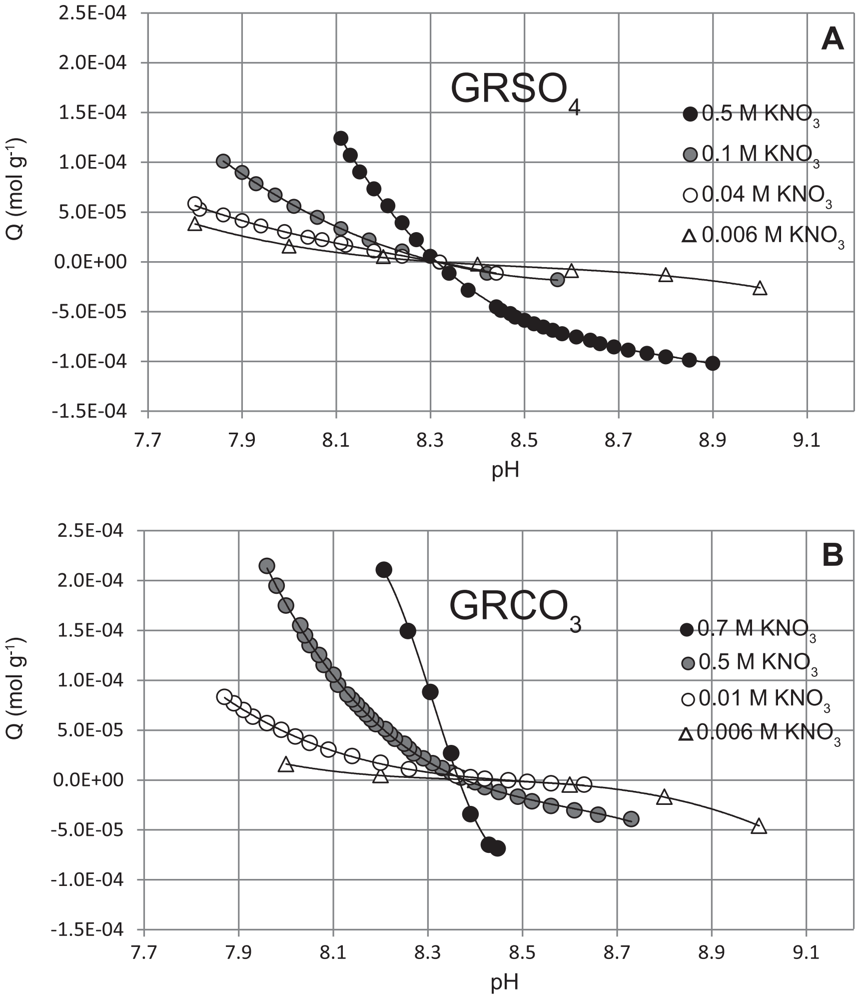

Fig. 5. Charge balance Q (in mol g^{-1}) calculated from the proton titrations performed in various electrolytes for $GRSO_4$ (A) and $GRCO_3$ (B). Circles are the data obtained from traditional titrations using Eq. (5) on pre-weighed solid (black circles) or *in situ* precipitated minerals (grey and open circles). Open triangles were obtained from our developed protocol using Eq. (6). The point of zero charge is given by the common intersection point of the curves.

controls H^+ adsorption, as green rust is by far the dominant mineral species. This is further supported by the fact that no other observable Fe bearing phase participates in the XRD spectra, nor was detected in TEM analyses of the titration's end-products. Note that Fig. 4 was not used to determine GR solubility, but only to define what mechanism dominates GR solubility in order to estimate the amount of H^+ consumed during GR equilibrium dissolution using Eqs. (1) and (2). Overall, this estimation resulted in only a very minor correction to Eq. (5), as $[H^+]_c$ was 2 to 4 orders of magnitude smaller than C_A in Eq. (5).

3.4. Surface charge

The preliminary experiments following the method described by Ahmed and Maksimov (1969) and Tewari and McLean (1972) showed that no pH shift was observed after green rust addition to various electrolytes when the starting pH was 8.3 ± 0.2 and 8.5 ± 0.2 for $GRSO_4$ and $GRCO_3$, respectively. Since the difference between both species comes essentially from the anions in the interlayers, it is not surprising that the preliminary estimate of the PZC is, within error, essentially the same for both minerals. As explained above, however, this method only permitted us to narrow down the pH range of potentiometric titrations because it does not take into account any green rust dissolution or matrix effects.

Fig. 5 shows the surface charge for $GRSO_4$ and $GRCO_3$ calculated for different ionic strengths using the "traditional" titration curves (Eq. (5)) and the method we developed (Eq. (6)), using a stability criterion of 0.05 pH/min, since reducing it to 0.001 pH/min provoked significant hysteresis as pointed out by Kapetas et al. (2011). Note that we plotted the curves for which the back-titrations were matching, and where no phases other than green rust were detected in the recovered solid products at the end of the titration. We obtained a common intersection point using the different methods, implying that the data are of good quality and reproducible, and that PZC values are 8.3 ± 0.1and 8.35 ± 0.05 for $GRSO_4$ and $GRCO_3$, respectively. Variations in curve shapes using different electrolyte concentrations may be due to different extents of nitrate reduction, but although the surface site chemistry may be affected, the common intersection point for all curves suggests that nitrate reduction was not significant enough to affect the PZC.

3.5. Particle growth and ageing

TEM imaging revealed that the average diameter of freshly precipitated $GRCO_3$ and $GRSO_4$ hexagons was ~ 54 ± 13 nm ($n = 27$) when freshly precipitated. This is similar to the lower range of abiotic green rust particle sizes observed in previous studies, where particles vary from ~50 to ~200 nm (Ruby et al., 2003; Bocher et al., 2004; Ruby et al., 2006). Interestingly, applying the Scherrer equation to the first diffraction peak gave much smaller diameters for the minimum crystallite size (L, Table 1), of around ~20 nm (6–40 nm). This could be the result of shape effects whereby the spherical shape parameter (k) in the Scherrer equation may be inappropriate for hexagonal particles. Alternatively, due to the very platy morphology of green rust and using {001} as the measured reflection peak, L could reflect the size of the shortest dimension of the particles rather than the average hexagon diameter, as in their high resolution TEM imaging, Bocher et al. (2004) showed that for ~90 nm hexagons, the particle thickness is ~15 nm(i.e. very similar to that observed in our experiments).Note that the effects on glycerol on green rust crystallinity are not known, and it is envisaged that discrepancies between observed (TEM derived) and calculated (Scherrer derived) sizes result from these potential effects. Regardless of this, our aim here was to inspect the evolution of green rust particles through time.

XRD scans of aged material shows an increase in peak intensity with time, as showed with $GRCO_3$ in Fig. 6A. Narrowing of peaks implies an increase in the mineral crystallinity and size of the domains. Table 1 documents the evolution of the full width of the peak at half maximum (FWHM) and calculated L with time. Both green rust types seem to display slight size differences, but both grow at comparable rates. L increases rapidly within the first 50 min, whereas after 200 min, it seems to reach the asymptotic value of ~30 and ~40 nm for $GRCO_3$ and $GRSO_4$, respectively. Fig. 6B shows that after 8 h of ageing, the diffraction peaks for green rust decrease in intensity and broaden, and diffraction peaks for magnetite appear and increase in intensity with time. After 69 h, green rust almost completely disappears from the diffractogram in favour of magnetite (See Supplementary Information 3 for further supporting data regarding GR-magnetite transformations).

4. DISCUSSION

4.1. Surface chemistry of green rust particles

As explained above, the difference between type 1 and type 2 green rusts lies in the nature of the interlayer anions and crystal geometry. Because the surface charge is determined by the Fe hydroxide layer, it is not surprising that within error, the PZC at the surface of both green rust species is the same. For pH > ~8.3, available sites at the surface of $GRCO_3$ and $GRSO_4$ sum to an overall negative charge, whereas for pH < ~8.3, the sum of available sites gives a positive surface charge. This is in good agreement with literature data on pH dependent green rust adsorption, as Jönsson and Sherman (2008) showed that arsenate desorbs from green rust for pH > 8, and chromate reduction by $GRCO_3$ is enhanced at lower pH (i.e. when chromate adsorption to the positively charged GR surface is favoured, Williams and Scherer, 2001). Recent studies on nitrate reduction by chlorinated and fluorinated GR (Choi and Batchelor, 2008; Choi et al., 2012) have shown that ammonium production is "delayed" when pH increases. Our results suggest that for pH > 8.3, nitrate adsorption is minimised and subsequent reduction occurs at slower rates.

At the surface of Fe (oxyhydr)oxides, reactive surface sites are comprised of the hydroxyl groups. Previous studies on $GRCO_3$ (Bocher et al., 2004) and $GRSO_4$ (Jönsson and Sherman, 2008) have shown that the basal, hexagonal

Table 1
XRD crystal peak parameters and associated sizes (calculated from Eq. (7)) throughout ageing experiments (<250 min).

$GRCO_3$			$GRSO_4$		
t (min)	FWHM (Å)	L (nm)	t (min)	FWHM (Å)	L (nm)
6.0	1.44	6.09	5.0	0.82	11.54
15.0	0.93	9.96	15.0	0.55	18.96
37.0	0.62	16.15	29.5	0.48	22.75
37.0	0.58	17.73	61.0	0.40	29.50
62.0	0.51	21.28	6.0	0.58	11.70
123.0	0.47	23.75	12.0	0.52	20.42
175.0	0.42	27.14	30.0	0.44	25.69
235.0	0.38	31.42	77.0	0.39	30.63
6.0	1.54	5.65	120.0	0.38	31.86
15.0	0.74	13.06	240.0	0.33	40.12
21.0	0.76	12.67			
25.0	0.71	13.66			
64.0	0.62	16.25	Precision on L (1σ)±1.4 nm		
122.0	0.49	22.23			

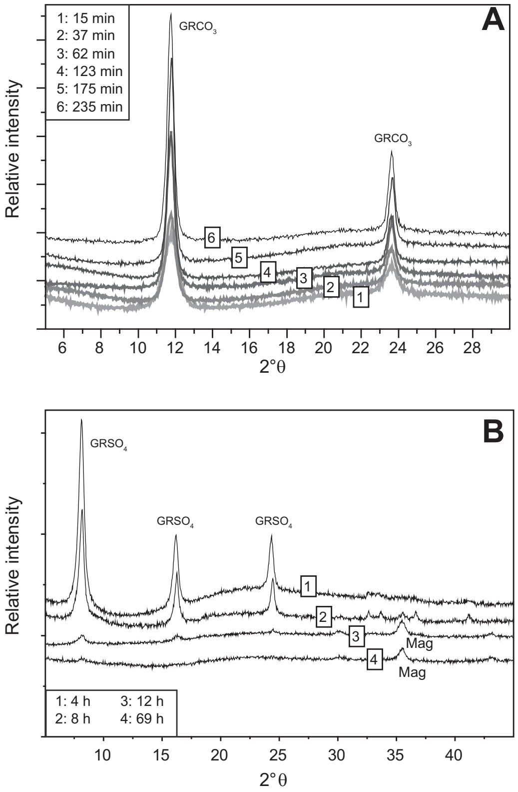

Fig. 6. XRD spectra showing an increase in crystallinity (increase in peak height and decrease in peak broadening) during the first 250 min of $GRCO_3$ ageing (A). Long term ageing (>4 h) leads to the conversion of GR to magnetite, as exemplified for $GRSO_4$ by the decrease of GR peaks and the appearance of magnetite peaks (B).

{0 0 1} face is comprised entirely of tri-coordinated hydroxyl sites, whereas the lateral {0 1 0} and {1 0 0} faces are comprised of a mixture of tri-, doubly- and mono-coordinated hydroxyl sites. In order to resolve the contribution of each Fe(II) and Fe(III) to hydroxyl groups, Bocher et al. (2004) showed that the brucite-like structure of the hydroxide layers can be written as $[Fe^{II}_{2/3}(OH)_{4/3}][Fe^{III}_{1/3}(OH)_{2/3}]^{1/3+}$, whereby the Pauling's valence charge for each Fe(II) and Fe(III) species is +1/3. Bocher et al. (2004) listed the formal surface charge of the various hydroxyl sites as: $\equiv FeOH^{-2/3}$, $\equiv Fe_2OH^{-1/3}$ and $\equiv Fe_3OH^0$. $\equiv Fe_3OH^0$ is the strongly acidic, tri-coordinated site that can protonate and deprotonate (Eqs. (12) and (13)), $\equiv Fe_2OH^{-1/3}$ is the doubly-coordinated site that can protonate (Eq. (14)), and $\equiv FeOH^{-2/3}$is the mono-coordinated site that can protonate (Eq. (15)). Deprotonation reactions for the doubly- and mono-coordinated sites are unlikely to occur since the resulting deprotonated species would be unstable according to Pauling's valence.

$$Fe_3OH^0 + H^+ = Fe_3OH_2^+ \quad \log K_{tri1} = 8.3 \tag{12}$$

$$Fe_3OH^0 = Fe_3O^- + H^+ \quad \log K_{tri2} = 8.3 \tag{13}$$

$$Fe_2OH^{-1/3} + H^+ = Fe_2OH_2^{+2/3} \quad \log K_{doubly1} = 8.2 \tag{14}$$

$$FeOH^{-2/3} + H^+ = FeOH_2^{+1/3} \quad \log K_{mono1} = 8.3 \tag{15}$$

Table 2
Crystallographic and complexation parameters used for the surface complex modelling.

Hexagonal crystal		
Radius (nm)	45	
Thickness (nm)	15	
{0 0 1} Fe atoms per m^2 (at/m^2)	1.19×10^{19}	Bocher et al. (2004)
{0 1 0} Fe atoms per m^2 (at/m^2)	1.37×10^{18}	Bocher et al. (2004)
Total specific area (m^2/g)	47	Williams and Scherer (2001)
Fe(II) or Fe(III) tri-coordinated OH species	$\equiv Fe_3OH^0$	Bocher et al. (2004)
Fe(II) or Fe(III) doubly-coordinated OH species	$\equiv Fe_2OH^{-1/3}$	Bocher et al. (2004)
Fe(II) or Fe(III) mono-coordinated OH species	$\equiv FeOH^{-2/3}$	Bocher et al. (2004)

Jönsson and Sherman (2008) proposed that the tri-coordinated sites of the $GRSO_4$ {0 0 1} faces are unreactive to anion adsorption since this would imply OH^- substitution from the strongly acidic $\equiv Fe_3OH^0$. This assumption can also be considered valid for $GRCO_3$ as Bocher et al. (2004) report EDX-TEM evidence to suggest that phosphate did not adsorb to the {0 0 1} surface. Since the {0 0 1} surface comprises the majority of surface sites, this finding suggests that green rust adsorption is restricted to the lateral {0 1 0} and {1 0 0} surface sites. However, the consequences of this are different for cation adsorption, since increasing pH would promote $\equiv Fe_3OH^0$ deprotonation (Eq. (13)), leading to a significant increase in available adsorption sites.

Surface complexation was modelled in Phreeqc Interactive 2.15.0 using the generalised electric two-layer model described in Dzombak and Morel (1990). We developed the model for $GRCO_3$as the crystallographic parametersare available (Williams and Scherer, 2001; Bocher et al., 2004) and are summarised in Table 2. We assumed an even repartitioning of the different sites along the lateral {0 1 0} and {1 0 0} faces, and used the Fe atom density data from Bocher et al. (2004) and the BET-measured specific surface area for $GRCO_3$ from Williams and Scherer (2001). For each pH step, site concentration was calculated and Q was derived from Eq. (16):

$$Q_{model} = [\equiv Fe_3OH_2^+] - [\equiv Fe_3O^-] - [\equiv Fe_2OH^{-1/3}] + [\equiv Fe_2OH_2^{+2/3}] - [\equiv FeOH^{-2/3}] + [\equiv FeOH_2^{+1/3}] \tag{16}$$

The set of apparent surface reaction constants (Eqs. (12)–(15)) was modified stepwise until we obtained a best fit between the derived model and the proton titration data for a total ionic strength of 0.006 M. Fig. 7 illustrates a proposed surface complexation model which describes the net charge of $GRCO_3$ surface with varying pH. Note that due to the relative surface area of the {0 0 1} face, the dominant complexes are the tri-coordinated species (Fig. 7B).The model is a simplification in that it does not account for non-stoichiometries or surface heterogeneities. It also disregards

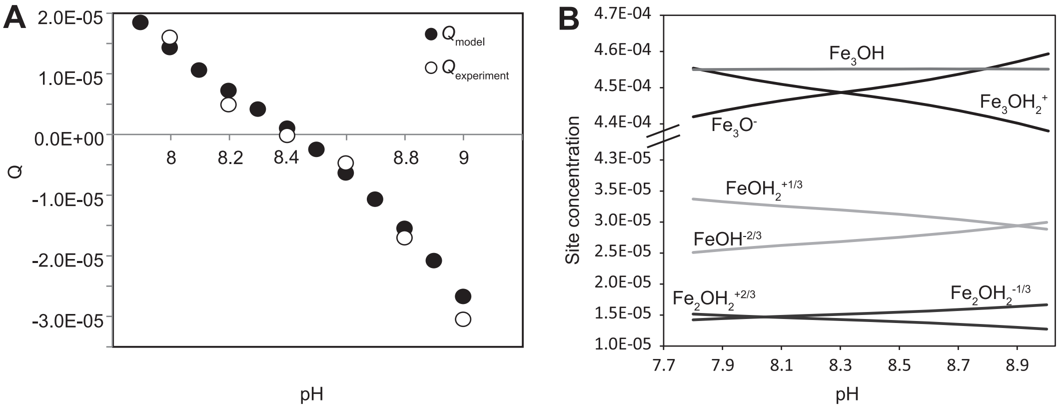

Fig. 7. Best fit between experimental (open circles) and model (black circles) derived charge balances for $GRCO_3$ and an ionic strength of 0.006 M (A) and associated surface complexation (B). Site concentration is in mol g^{-1}.

the effects of various extents of nitrate reduction on the reactive sites which may occur as suggested by the shape differences of the titration curves. However, it does link for the first time the previously established surface site characteristics of green rust, with the net surface charge of particles in aqueous media.

4.2. Formation and growth of green rust particles

The size of freshly precipitated abiotic particles depends upon experimental protocols, and in our experiments, $GRCO_3$ and $GRSO_4$ precipitated in the lower range of sizes for abiotic green rust. Interestingly, green rust crystals produced during biologically mediated reactions tend to display much larger sizes, up to tens of microns (e.g. Zegeye et al., 2005; Berthelin et al., 2006; Zegeye et al., 2010). The size of precipitated green rust is important since the rates and mechanisms of particle growth are size dependent. Two mechanisms are usually proposed to describe the rate of particle growth in aqueous media: growth by oriented aggregation and by Ostwald-ripening. Aggregation-growth, which permits a decrease in surface energy, has been demonstrated for a number of geologically relevant nanoparticulate materials, including Fe oxyhydroxides, Ti oxides, and metal sulphides (e.g. Penn and Banfield, 1998, 1999; Banfield et al., 2000; Banfield and Zhang, 2001; Penn et al., 2001; Huang et al., 2003; Zhang and Banfield, 2004; Waychunas et al., 2005; Guilbaud et al., 2010). Such a growth mechanism has wide consequences for the chemical behaviour of nanoparticles in solution, and for the retention of toxic metals as they may be trapped within the particle structure during aggregation. On the other hand, Ostwald-ripening is characterised by the dissolution of smaller particles in favour of larger ones, implying that during growth, adsorbed ions will be released into solution and re-adsorbed or co-precipitated at the surface of larger particles.

The rate equations for both mechanisms have been determined. Huang et al. (2003) developed a crystal growth model for aggregation-growth using Scherrer derived size data for ZnS nanoparticles (Eq. (17)):

$$D = \frac{D_0({}^{3}\sqrt[3]{2}kt + 1)}{(kt + 1)} \tag{17}$$

where D is the average diameter (the subscript *0* meaning "initial"), t is the time and k a constant.

For the Ostwald ripening mechanism, the evolution in particle size is given by Eq. (18) (Joesten, 1991):

$$D - D_0 = k(t - t_0)^{1/n} \tag{18}$$

where n is an integer describing the physical mechanism, usually comprised between 2 and 5. Parameters k and n can be extracted using the logarithm of Eq. (18) in a *ln* $(D - D_0)$ versus *ln* $(t - t_0)$ plot.

Fig. 8 compares the experimental results with the particle size prediction obtained during Ostwald-ripening (Eq. (18)), and our data suggest that both green rust species may grow via Ostwald ripening. In contrast, the aggregation-growth model (not shown) gave non supporting results, with final mineral sizes (250 min) converging asymptotically towards ~10 nm. This suggests that during

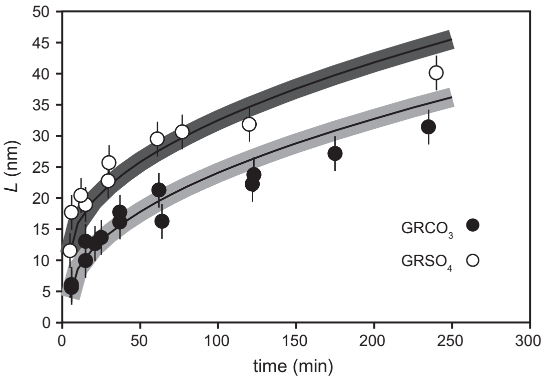

Fig. 8. Evolution of the lowest crystallite average size (L) calculated from Eq. (7) for both green rust species (open and black circles) through time. Error bars are shown on a 2σ level. Solid lines represent the predicted size evolution using an Ostwald ripening model. Shadows represent the error envelopes on the model, calculated using a 2σ precision.

the growth of $GRCO_3$ and $GRSO_4$, small particles dissolve back into solution and re-precipitate at the surface of larger particles, implying similar dynamics for any adsorbed species. This might result in a larger uptake of dissolved species as both adsorption and co-precipitation occur during Ostwald-ripening. Note that the highest rates of GR growth occur within the first 50 min as shown in Fig. 8. The exact behaviour of potential adsorbed/desorbed metals or other contaminants during the very first stages of particle growth is yet to be investigated. After 200 min, however, the growth rate seems to decrease towards an asymptote, after L has increased by >3. When converting into a volume, this constitutes a substantial proportion of the total growth (See Supplementary Information 4 for further discussion regarding use of the Scherrer equation to determine the growth mechanism).

After 8 h of ageing we noted the transformation of green rust into magnetite. This is entirely consistent with a recent study of green rust formation in an anoxic Fe-rich water column, whereby magnetite was also found forming in the water column (Zegeye et al., 2012). Whether adsorbed and/or incorporated metals can transfer to magnetite, or are released as dissolved ions in the aqueous media, is unclear, although studies of green rust and magnetite formation during bacterial reduction of hydrous ferric oxide have suggested that the ionic forms of elements such as P and Ni are not effectively removed from solution during magnetite growth (Parmar et al., 2001). The role of green rust transformation pathways on the non-reversible removal of contaminants and bioessential nutrients (e.g. Jönsson and Sherman, 2008; Zegeye et al., 2012) from solution clearly requires further detailed study.

5. CONCLUSIONS

We have determined the net surface charge of sulphated and carbonated green rust by potentiometric titrations. The point of zero charge for both species is ~8.3. This implies that marine environments and alkaline settings favour negatively charged particle surfaces, enhancing cation adsorption over anion adsorption. As confirmed by previous studies, this impacts directly upon the rates and the extent of subsequent reduction of adsorbed species (e.g. Williams and Scherer, 2001; Jönsson and Sherman, 2008). This has wide implications for the removal of contaminants or nutrients from solution, since under anoxic, non-sulphidic conditions, green rust may be a prevalent Fe bearing authigenic mineral phase (Zegeye et al., 2012).

The adsorption of dissolved ions to green rust is, however, more complicated than that suggested by a simple pH-dependent ion fixation. Our data demonstrate for the first time that green rust particles grow via an Ostwald-ripening mechanism, implying that adsorbed species are likely to be subject to repetitive steps of release into solution and re-adsorption during the dissolution–reprecipitation mechanism. Conversion of metastable green rust into the more stable magnetite phase may also have further effects on the partitioning of adsorbed and dissolved ions, but these potential effects are yet to be fully explored.

ACKNOWLEDGEMENTS

We are thankful to Leon Kapetas, Asfaw Zegeye, Christian Ruby, Frédéric Jorand and three anonymous reviewers for constructive discussions which significantly improved the quality of the manuscript. We also thank Berni Bowler, Kath White and Tracey Davey for technical support. This work was funded by NERC through the “Co-Evolution of Life and the Planet” scheme.

APPENDIX A. SUPPLEMENTARY DATA

Supplementary data associated with this article can be found, in the online version, at http://dx.doi.org/10.1016/j.gca.2013.01.017.

REFERENCES

Abdelmoula M., Trolard F., Bourrié G. and Génin J. M. R. (1998) Evidence for the Fe(II)–Fe(III) green rust “fougerite” mineral occurrence in a hydromorphic soil and its transformation with depth. *Hyperfine Interactions* **112**, 235–238.

Ahmed S. M. and Maksimov D. (1969) Studies of the double layer on cassiterite and rutile. *Journal of Colloid and Interface Science* **29**, 97–104.

Ahmed I. A. M., Benning L. G., Kakonyi G., Sumoondur A. D., Terrill N. J. and Shaw S. (2010) Formation of green rust sulfate: a combined in situ time-resolved X-ray scattering and electrochemical study. *Langmuir* **26**(9), 6593–6603.

Antelo J., Avena M., Fiol S., López R. and Arce F. (2005) Effects of pH and ionic strength on the adsorption of phosphate and arsenate at the goethite–water interface. *Journal of Colloid and Interface Science* **285**, 476–486.

Banfield J. F. and Zhang H. (2001) Nanoparticles in the environment. *Reviews in Mineralogy and Geochemistry* **44**, 1–58.

Banfield J. F., Welch S. A., Zhang H., Ebert T. T. and Penn R. L. (2000) Aggregation-based crystal growth and microstructure development in natural iron oxyhydroxidebiomineralization products. *Science* **289**, 751–754.

Bebié J., Schoonen M. A. A., Fuhrmann M. and Strongin D. R. (1998) Surface charge development on transition metal sulfides: an electrokinetic study. *Geochimica et Cosmochimica Acta* **62**, 633–642.

Berthelin J., Ona-Nguema G., Stemmler S., Quantin C., Abdelmoula M. and Jorand F. (2006) Bioreduction of ferric species and biogenesis of green rusts in soils. *Comptes Rendus Geoscience* **338**, 447–455.

Bocher F., Géhin A., Ruby C., Ghanbaja J., Abdelmoula M. and Génin J.-M. R. (2004) Coprecipitation of Fe(II–III) hydroxycarbonate green rust stabilised by phosphate adsorption. *Solid State Sciences* **6**, 117–124.

Bond D. L. and Fendorf S. (2003) Kinetics and structural constraints of chromate reduction by green rusts. *Environmental Science and Technology* **37**, 2750–2757.

Brindley G. W. (1980) Order-disorder in clay mineral structures. In *Crystal Structures of Clay Minerals and their X-ray Identification* (eds. G. W. Brindley and G. Brown). Mineralogical Society London. pp. 125–195.

Butler I. B., Schoonen M. A. A. and Rickard D. T. (1994) Removal of dissolved oxygen from water: a comparison of four common techniques. *Talanta* **41**, 211–215.

Choi J. and Batchelor B. (2008) Nitrate reduction by fluoride green rust modified with copper. *Chemosphere* **70**, 1108–1116.

Choi J., Batchelor B., Won C. and Chung J. (2012) Nitrate reduction by green rusts modified with trace metals. *Chemosphere* **86**, 860–865.

Christiansen B. C., Balic-Zunic T., Dideriksen K. and Stipp S. L. S. (2009) Identification of green rust in groundwater. *Environmental Science and Technology* **43**, 3436–3441.

Drissi S. H., Refait P., Abdelmoula M. and Génin J. M. R. (1995) The preparation and thermodynamic properties of Fe(II)–Fe(III) hydroxide-carbonate (green rust 1); Pourbaix diagram of iron in carbonate-containing aqueous media. *Corrosion Science* **37**, 2025–2041.

Dzombak D. A. and Morel F. (1990) *Surface Complexation Modelling: Hydrous Ferric Oxide*. Wiley-Interscience, p. 393.

Erbs M., Bruun Hansen H. C. and Olsen C. E. (1998) Reductive dechlorination of carbon tetrachloride using iron(II) iron(III) hydroxide sulfate (green rust). *Environmental Science and Technology* **33**, 307–311.

Géhin A., Ruby C., Abdelmoula M., Benali O., Ghanbaja J., Refait P. and Génin J.-M. R. (2002) Synthesis of Fe(II–III) hydroxysulphate green rust by coprecipitation. *Solid State Sciences* **4**, 61–66.

Génin J.-M. R., Refait P., Bourrié G., Abdelmoula M. and Trolard F. (2001) Structure and stability of the Fe(II)–Fe(III) green rust "fougerite" mineral and its potential for reducing pollutants in soil solutions. *Applied Geochemistry* **16**, 559–570.

Guilbaud R., Butler I. B., Ellam R. M. and Rickard D. (2010) Fe isotope exchange between Fe(II)aq and nanoparticulatemackinawite (FeSm) during nanoparticle growth. *Earth and Planetary Science Letters* **300**, 174–183.

Hansen H. C. B. (1989) Composition, stabilization, and light adsorption of Fe(II)Fe(III) hydroxycarbonate (green rust). *Clay Minerals* **24**, 663–669.

Hansen H. C. B. and Koch C. B. (1998) Reduction of nitrate to ammonium by sulphate green rust: activation energy and reaction mechanism. *Clay Minerals* **33**, 87–101.

Hansen H. C. B., Guldberg S., Erbs M. and Bender Koch C. (2001) Kinetics of nitrate reduction by green rusts – effects of interlayer anion and Fe(II):Fe(III) ratio. *Applied Clay Science* **18**, 81–91.

Huang F., Zhang H. and Banfield J. F. (2003) Two-stage crystal-growth kinetics observed during hydrothermal coarsening of nanocrystalline ZnS. *Nano Letters* **3**, 373–378.

Jeong H. Y., Lee J. H. and Hayes K. F. (2008) Characterization of synthetic nanocrystalline mackinawite: crystal structure, particle size, and specific surface area. *Geochimica et Cosmochimica Acta* **72**, 493–505.

Joesten R. (1991). Grain-boundary diffusion kinetics in silicates and oxide minerals. In *Diffusion, Atomic Ordering, and Mass Transport. Adv. Phys. Chem.* (ed. J. Ganguly). vol. **8**, pp. 345–395.

Jönsson J. and Sherman D. M. (2008) Sorption of As(III) and As(V) to siderite, green rust (fougerite) and magnetite: implications for arsenic release in anoxic groundwaters. *Chemical Geology* **255**, 173–181.

Kapetas L., Ngwenya B. T., Macdonald A. M. and Elphick S. C. (2011) Kinetics of bacterial potentiometric titrations: the effect of equilibration time on buffering capacity of Pantoea agglomerans suspensions. *Journal of Colloid and Interface Science* **359**, 481–486.

Kappler A. and Newman D. K. (2004) Formation of Fe(III)-minerals by Fe(II)-oxidizing photoautotrophic bacteria. *Geochimica et Cosmochimica Acta* **68**, 1217–1226.

Lee W. and Batchelor B. (2002) Abiotic reductive dechlorination of chlorinated ethylenes by iron-bearing soil minerals. 2. Green rust. *Environmental Science and Technology* **36**, 5348–5354.

Legrand L., El Figuigui A., Mercier F. and Chausse A. (2004) Reduction of aqueous chromate by Fe(II)/Fe(III) carbonate green rust: kinetic and mechanistic studies. *Environmental Science and Technology* **38**, 4587–4595.

Loyaux-Lawniczak S., Refait P., Ehrhardt J.-J., Lecomte P. and Génin J.-M. R. (1999) Trapping of Cr by formation of ferrihydrite during the reduction of chromate ions by Fe(II)–Fe(III) hydroxysalt green rusts. *Environmental Science and Technology* **34**, 438–443.

Myneni S. C. B., Tokunaga T. K. and Brown G. E. (1997) Abiotic selenium redox transformations in the presence of Fe(II, III) oxides. *Science* **278**, 1106–1109.

Ona-Nguema G., Abdelmoula M., Jorand F., Benali O., Block J.-C. and Génin J.-M. R. (2001) Iron(II, III) hydroxycarbonate green rust formation and stabilization from lepidocrocite bioreduction. *Environmental Science and Technology* **36**, 16–20.

Pantke C., Obst M., Benzerara K., Morin G., Ona-Nguema G., Dippon U. and Kappler A. (2012) Green rust formation during Fe(II) oxidation by the nitrate-reducing acidovorax sp. strain BoFeN1. *Environmental Science and Technology* **46**, 1439–1446.

Parmar N., Gorby Y. A., Beveridge T. J. and Ferris F. G. (2001) Formation of green rust and immobilization of nickel in response to bacterial reduction of hydrous ferric oxide. *Geomicrobiology Journal* **18**, 375–385.

Penn R. L. and Banfield J. F. (1998) Imperfect oriented attachment: dislocation generation in defect-free nanocrystals. *Science* **281**, 969–971.

Penn R. L. and Banfield J. F. (1999) Morphology development and crystal growth in nanocrystalline aggregates under hydrothermal conditions: insights from titania. *Geochimica et Cosmochimica Acta* **63**, 1549–1557.

Penn R. L., Oskam G., Strathmann T. J., Searson P. C., Stone A. T. and Veblen D. R. (2001) Epitaxial assembly in aged colloids. *J. Phys. Chem. B* **105**, 2177–2182.

Poulton S. W., Krom M. D. and Raiswell R. (2004) A revised scheme for the reactivity of iron (oxyhydr)oxide minerals towards dissolved sulfide. *Geochimica et Cosmochimica Acta* **68**, 3703–3715.

Randall S. R., Sherman D. M. and Ragnarsdottir K. V. (2001) Sorption of As(V) on green rust (Fe4(II)Fe2(III)(OH)12SO_4·$3H_2O$) and lepidocrocite (γ-FeOOH): surface complexes from EXAFS spectroscopy. *Geochimica et Cosmochimica Acta* **65**, 1015–1023.

Refait P., Drissi S. H., Pytkiewicz J. and Génin J.-M. R. (1997) The anionic species competition in iron aqueous corrosion: role of various green rust compounds. *Corrosion Science* **39**, 1699–1710.

Refait P., Abdelmoula M. and GÉnin J.-M. R. (1998) Mechanisms of formation and structure of green rust one in aqueous corrosion of iron in the presence of chloride ions. *Corrosion Science* **40**, 1547–1560.

Refait P., Bon C., Simon L., Bourrie G., Trolard F., Bessiere J. and Genin J. M. R. (1999) Chemical composition and Gibbs standard free energy of formation of Fe(II)–Fe(III) hydroxysulphate green rust and Fe(II) hydroxide. *Clay Minerals* **34**, 499–510.

Rickard D. and Luther G. W. (2007) Chemistry of iron sulfides. *Chemical Reviews* **107**, 514–562.

Ruby C., Géhin A., Abdelmoula M., Génin J.-M. R. and Jolivet J.-P. (2003) Coprecipitation of Fe(II) and Fe(III) cations in sulphated aqueous medium and formation of hydroxysulphate green rust. *Solid State Sciences* **5**, 1055–1062.

Ruby C., Aïssa R., Géhin A., Cortot J., Abdelmoula M. and Génin J.-M. (2006a) Green rusts synthesis by coprecipitation of FeII–FeIII ions and mass-balance diagram. *Comptes Rendus Geoscience* **338**, 420–432.

Ruby C., Upadhyay C., Géhin A., Ona-Nguema G. and Génin J.-M. R. (2006b) In situ redox flexibility of FeII–III oxyhydroxycarbonate green rust and fougerite. *Environmental Science and Technology* **40**, 4696–4702.

Schikorr G. (1933) ÜberEisen(II)-hydroxyd und einferromagnetischesEisen(III)-hydroxyd. *Zeitschrift fur Anorganische und Allgemeine Chemie* **212**, 33–39.

Schwertmann U. and Fechter H. (1994) The formation of green rust and its transformation to lepidocrocite. *Clay Minerals* **29**, 87–92.

Simon L., François M., Refait P., Renaudin G., Lelaurain M. and Génin J.-M. R. (2003) Structure of the Fe(II–III) layered double hydroxysulphate green rust two from Rietveld analysis. *Solid State Sciences* **5**, 327–334.

Stampfl P. P. (1969) Einbasischeseisen-II–III-karbonat in rost. *Corrosion Science* **9**, 185–187.

Świetlik J., Raczyk-Stanisławiak U., Piszora P. and Nawrocki J. (2012) Corrosion in drinking water pipes: the importance of green rusts. *Water Research* **46**, 1–10.

Tewari P. H. and McLean A. W. (1972) Temperature dependence of point of zero charge of alumina and magnetite. *Journal of Colloid and Interface Science* **40**, 267–272.

Trolard F., Génin J.-M. R., Abdelmoula M., Bourrié G., Humbert B. and Herbillon A. (1997) Identification of a green rust mineral in a reductomorphic soil by Mossbauer and Raman spectroscopies. *Geochimica et Cosmochimica Acta* **61**, 1107–1111.

Usman, M., Hanna, K., Abdelmoula, M., Zegeye, A., Faure, P., Ruby, C., in press.Formation of green rust via mineralogical transformation of ferric oxides (ferrihydrite, goethite and hematite). *Applied Clay Science*.

Vinš J., Šubrt J., Zapletal V. and Hanousek F. (1987) Preparation and properties of green rust type substances. *Collection of Czechoslovak Chemical Communications* **52**, 93–102.

Vogel A. I. (1951) *A Text-Book of Quantitative Inorganic Analysis, Therory and Practice*, second ed. Longmans, Green and Co..

Warren B. E. (1990) *X-ray Diffraction*. Dover Publications, Inc., New York (Dover edition, originally published in Addison–Wesley series in Metallurgy and Materials, M. Cohen, eds) p. 381.

Waychunas G. A., Kim C. S. and Banfield J. F. (2005) Nanoparticulate iron oxide minerals in soils and sediments: unique properties and contaminant scavenging mechanisms. *Journal of Nanoparticle Research* **7**, 409–433.

Widler A. M. and Seward T. M. (2002) The adsorption of gold(I) hydrosulphide complexes by iron sulphide surfaces. *Geochimica et Cosmochimica Acta* **66**, 383–402.

Williams A. G. B. and Scherer M. M. (2001) Kinetics of Cr(VI) reduction by carbonate green rust. *Environmental Science and Technology* **35**, 3488–3494.

Wolthers M., van der Gaast S. J. and Rickard D. (2003) The structure of distoredmackinawite. *American Mineralogist* **88**, 2007.

Wolthers M., Charlet L., van der Linde P. R., Rickard D. and van der Weijden C. H. (2005) Surface chemistry of disordered mackinawite (FeS). *Geochimica et Cosmochimica Acta* **69**, 3469–3481.

Zegeye A., Ona-Nguema G., Carteret C., Huguet L., Abdelmoula M. and Jorand F. (2005) Formation of hydroxysulphate green rust 2 as a single iron(II–III) mineral in microbial culture. *Geomicrobiology Journal* **22**, 389–399.

Zegeye A., Ruby C. and Jorand F. (2007a) Kinetic and thermodynamic analysis during dissimilatory γ-FeOOH reduction: formation of green rust 1 and magnetite. *Geomicrobiology Journal* **24**, 51–64.

Zegeye A., Huguet L., Abdelmoula M., Carteret C., Mullet M. and Jorand F. (2007b) Biogenic hydroxysulfate green rust, a potential electron acceptor for SRB activity. *Geochimica et Cosmochimica Acta* **71**, 5450–5462.

Zegeye A., Mustin C. and Jorand F. (2010) Bacterial and iron oxide aggregates mediate secondary iron mineral formation: green rust versus magnetite. *Geobiology* **8**, 209–222.

Zegeye A., Bonneville S., Benning L. G., Sturm A., Fowle D. A., Jones C., Canfield D. E., Ruby C., MacLean L. C., Nomosatryo S., Crowe S. A. and Poulton S. W. (2012) Green rust formation controls nutrient availability in a ferruginous water column. *Geology* **40**, 599–602.

Zhang H. and Banfield J. F. (2004) Aggregation, coarsening, and phase transformation in ZnS nanoparticles studied by molecular dynamics simulations. *Nano Letters* **4**, 713–718.

Associate editor: Liane G. Benning